Testing Symmergent gravity through the shadow image and weak field photon deflection by a rotating black hole using the M87* and Sgr. A* results

Reggie C. Pantig,1,* Ali Övgün,2,† and Durmuş Demir3,‡

¹Physics Department, De La Salle University, 2401 Taft Avenue, Manila, 1004 Philippines

²Physics Department, Eastern Mediterranean University,
Famagusta, 99628 North Cyprus via Mersin 10, Turkey

³Faculty of Engineering and Natural Sciences, Sabanci University, 34956 İstanbul, Turkey

(Dated: August 8, 2022)

Motivated by recent work on the Symmergent black hole [Phys. Dark Univ. 10.1016/j.dark.2021.100900, 2021], here we study spinning black holes in Symmergent gravity, with spin parameter a. The goal is to uncover the deviations caused by the Symmergent gravity parameters relative to the known Kerr solution. To this aim, we first investigate the deviations in the photon sphere and shadow size. The EHT data was used to find constraints to c_0 that fit well in M87* within $\pm 1\sigma$ than in Sgr. A*. We also found that depending on the sign of the quadratic curvature coefficient c_0 , the increase in photon radius results in a decrease in shadow radius. Exploring the Symmergent effects on the geodesics of time-like particles, we find that these are more sensitive to the effects than null particles. To broaden the scope of the study, we also analyzed the weak field limit of the deflection angles, where we used the Gauss-Bonnet theorem with the consideration of the finite distance of the source and the receiver to the lensing object. We have shown how the Symmergent gravity parameter c_0 , which is proportional to the number difference between fermions and bosons affects the deflection angle. Remarkably, the distance of the receiver (or source) greatly affects the angle. Finally, we also analyze the Symmergent gravity effects on the rotating black hole as it acts as a particle accelerator.

PACS numbers: 95.30.Sf, 04.70.-s, 97.60.Lf, 04.50.Kd

Keywords: Black hole; Modified gravity; Geodesics; Weak gravitational lensing; Shadow; Deflection angle.

I. INTRODUCTION

In this work, we test a recent emergent gravity model with the shadow and deflection angle of rotating black holes using the observational data on the M87* and SgrA* black holes. The emergent gravity model we study exhibits distinctive signatures, as we have revealed in recent work on static black hole spacetimes [1]. It is expected that the rotating black hole spacetimes can act as a richer laboratory to test or explore the emergent gravity model we consider.

Fundamentally, quantum field theory (QFT) is intrinsic to flat spacetime simply because it rests on a Poincaré-invariant (translation-invariant) vacuum state [2, 3]. (Mass and spin of a particle are Casimir invariants.) Flat spacetime means the total absence of gravity. Incorporation of gravity necessitates the QFT to be transferred to curved spacetime, but this is hampered by Poincaré breaking in curved spacetime [3, 4]. This obstacle, plus the absence of a quantum theory of gravity [5] leads one to the emergent gravity [6–8] as a viable framework.

In general, loss of Poincaré invariance could be interpreted as the emergence of gravity into the QFT [9]. In a QFT, the curvature can emerge through Poincaré breaking sources, one example of which is the hard momentum cutoff. Indeed, an ultraviolet (UV) cutoff Λ [10] limits momenta p_{μ} within $-\Lambda^2 \leq \eta^{\mu\nu}p_{\mu}p_{\nu} \leq \Lambda^2$ as the intrinsic validity edge of the QFT [10]. It gives cause to scalar masses $(c_S\Lambda^2)$ and vacuum energy $(c_mm^2\Lambda^2+c_O\Lambda^4)$ at the loop level. It also gives cause to gauge boson masses $(c_V\Lambda^2)$ [11, 12], which break gauge symmetries explicitly since Λ is not a particle mass, that is, Λ is not a Casimir invariant of the Poincaré group. In Sakharov's induced gravity, Λ^2 is associated with the Planck scale, albeit with explicitly-broken gauge symmetries and Planckian-size cosmological constant and scalar masses.

In recent years, the induced gravity setup of Sakharov's been approached from a new perspective in which priority is given to the resolutions of the gauge symmetry breaking, Planckian-size scalar masses, and Planckian-size cosmological constant [13]. Given this priority, gravity has emerged so that the loop-induced gauge boson masses get erased, and scalar masses get stabilized by the curvature terms. This mechanism renders effective field theories natural regarding their destabilizing UV sensitivities. It gives rise to a new framework [13, 14] in which (i) its gravity sector is composed of the Einstein-Hilbert term plus a curvature-squared term, and (ii) its matter sector is an \overline{MS} -renormalized QFT [13]. This framework possesses distinctive signatures that can be searched via astrophysical, cosmological, and collider experiments. Its gravity sector, a symmetry-restoring emergent gravity

^{*} reggie.pantig@dlsu.edu.ph

[†] ali.ovgun@emu.edu.tr; https://www.aovgun.com

[‡] durmus.demir@sabanciuniv.edu

theory briefly termed as "Symmergent gravity" [14, 15], is composed entirely of loop-induced couplings, including Newton's constant G. Symmergent gravity is not a loop-induced curvature sector in curved spacetime [7, 16].

In contrast, the flat spacetime effective field theory is taken to curved spacetime [13, 14] in a way reviving the gauge symmetries broken explicitly by the UV cutoff. All of its couplings are loop-induced parameters deriving from the particle spectrum of the QFT (numbers and masses of particles). Thinking with respect to the standard model of known particles (leptons, quarks, gauge bosons, and the Higgs boson), new particles, necessary for inducing Newton's constant correctly, do not have to couple to the known particles. Using Occam's razor and stability of the Higgs boson mass, this freedom means that new particles do not couple to the known particles unless they are required to couple phenomenologically or experimentally [13, 17]. To exemplify this, one expects neutrinos to be Majorana since only such neutrinos keep the Higgs boson mass stable. The Symmergent gravity has already been studied in certain aspects. Its quadratic-curvature sector, different than that in [7, 16], has already been shown to give rise to the Starobinsky inflation [18]. Its very same quadratic curvature sector has recently been shown to possess distinctive signatures for the black hole shadow [1]. In more recent work, the Symmergent gravity has been studied in detail in the quasi-periodic oscillations, weak field lensing, and shadow cast around static black hole spacetimes [19]. We shall study Symmergent gravity in spinning black hole spacetimes in the present work. The present work (like the earlier ones [1, 18, 19]) can be viewed as "doing particle physics via black hole properties" as it will reveal salient features of the QFT sector through various black hole features.

In 1919 Arthur Eddington led an expedition to prove Einstein's theory of relativity using gravitational lensing, since then and has become an important tool in astrophysics [20–25]. In 2008, Gibbons and Werner used the Gauss-Bonnet theorem (GBT) on the optical geometries in asymptotically flat spacetimes and calculated the weak deflection angle first time in literature [26]. Afterwards, this method has been applied to various related phenomena [27–41]. One of the aims of this paper is to probe Symmergent gravity through the black hole's weak deflection angle using GBT and also shadow silhouette as perceived by a static remote observer. In essence, by the very Nature of the Symmergent gravity, we will be studying the numbers of fermions and bosons and other effects in the vicinity of a spinning black hole, which has the potential to affect the motions of null and time-like particles as well as its spin parameter a. (By definition, $a = cJ/GM^2$ where J and M are the angular momentum and mass of the rotation black hole.) Recently, the shadow coming from different black hole models has been analyzed extensively in the literature since the shadow can become a probe to the imprints of the astrophysical environment affecting it [42–89] The shadow cast calculation of a non-rotating black hole was pioneered by [90] and [91], and later on extended by [92] (and in Ref. [93]) to an axisymmetric spacetime. Recently, after the detection of gravitational waves in 2015 [94], the first image of the black hole in M87* was published by the Event Horizon Telescope (EHT) using the electromagnetic spectrum [95]. At this time of writing, new milestone has been achieved as the EHT revealed the shadow image of the black hole in our galaxy, Sgr. A* [96]. It only indicates that with how fast space technologies improve, the study of black hole theory is a scientific endeavor that cannot be underestimated.

The paper is organized as follows. In Sec. II, we briefly discuss the Symmergent gravity. Sect. III presents the rotating metric, which includes the Symmergent parameters. In Sect. IV, we studied the effect of Symmergent gravity on null geodesics, which in turn affects the shadow radius and observables associated with it. We also examined the said effect on time-like orbits in the same section. Then in Sect. V is devoted to investigating the weak deflection angle in finite-distance and in Sect. VI, we calculate the center-of-mass energy (CM) of two particles and study particle acceleration near rotating Symmergent black hole backgrounds. Sect. VII, we form conclusions and mention some related prospects of this study. All over this paper, we have used natural units by setting G = c = 1, and the metric signature (-, +, +, +).

II. SYMMERGENT GRAVITY

Symmergent gravity is essentially an $R+R^2$ gravity theory. It can be regarded as a special form of general f(R) gravity theories. It has been constructed in complete detail in [13] (see also [14, 15] for earlier discussions). It has recently been summarized in [1, 19] regarding its implications for black features like quasi-periodic oscillations, shadow radius, and weak lensing. These studies on Symmergent black holes give all the relevant details about the curvature sector of Symmergent gravity. Below, we briefly discuss the relevant features of the Symmergent gravity and refer the reader to [1, 13, 19] for other details.

The action functional governing the Symmergent gravity is given by

$$I[g] = \int d^4x \sqrt{-g} \left\{ \frac{R(g)}{16\pi G} - \frac{c_0}{16} R(g)^2 + \mathcal{L}_{matter} \right\}$$
 (1)

in which \mathcal{L}_{matter} is the part that contains all matter fields – the known ones in the standard model as well as the new ones needed to induce the Newton's constant as

$$\frac{1}{G} = \frac{\operatorname{str}\left[\mathcal{M}^2\right]}{8\pi} \tag{2}$$

where str[...] stands for the graded trace $str[\mathcal{M}^2] = \sum_s (-1)^s tr[\mathcal{M}^2]_s$, with s being the particle spin and \mathcal{M}^2 the mass-squared matrix of all the matter fields. Not only the Newton's constant but also the quadratic curvature coefficient

$$c_{\rm O} = \frac{n_{\rm B} - n_{\rm F}}{128\pi^2} \tag{3}$$

is a loop-induced parameter, with $n_{\rm B}$ ($n_{\rm F}$) standing for the total number of bosons (fermions) in the underlying QFT. Both the $n_{\rm B}$ bosons and $n_{\rm F}$ fermions contain not only the known standard model particles (quarks, leptons, photon, gluon, and weak bosons) but also completely new particles (massive as well as massless) that do not have to couple to the known particles non-gravitationally.

Before indulging into the analysis of the quadratic-curvature action (1) one notes that if the Nature contains equal numbers of the bosonic and fermionic degrees of freedom (namely, $n_{\rm B}=n_{\rm F}$) then $c_{\rm O}\equiv 0$. Then Symmergent gravity reduces to general relativity (with non-minimal couplings to scalars S in the theory). This bose-fermi symmetric structure is a property of the supersymmetric theories. Interestingly, symmergence predicts pure Einstein gravity when $n_{\rm B}=n_{\rm F}$ in Nature, with the further property that extra particles do not have to interact with the known particles. In this case, one obtains the usual asymptotically-flat Schwarzschild or Kerr black holes.

The curvature sector of the Symmergent gravity is an $R + R^2$ gravity, as already defined in action (1). The two model parameters, G and c_O , are purely loop-induced quantities, as explicitly given in in (2) and (3). The action (1) can be recast as

$$S = \frac{1}{16\pi G} \int d^4x \sqrt{-g} (R(g) - \pi G c_0 R(g)^2) , \qquad (4)$$

to have an f(R) gravity theory with

$$f(R) = R(g) - \pi G c_0 R(g)^2.$$

$$(5)$$

With this identification, the action (4) gives rise to the equation of motion

$$R_{\mu\nu}F(R) - \frac{1}{2}g_{\mu\nu}f(R) + [g_{\mu\nu}\Box - \nabla_{\mu}\nabla_{\nu}]F(R) = 0,$$
 (6)

in which □ is the d'Alembertian operator, and

$$F(R) = \frac{df(R)}{dR} = 1 - 2\pi G c_0 R \tag{7}$$

is the derivative of f(R) with respect to its argument. With the use of its trace over spacetime indices, the equation of motion (6) can be reexpressed in the form

$$R_{\mu\nu}F(R) - \frac{g_{\mu\nu}}{4}RF(R) + \frac{g_{\mu\nu}}{4}\Box F(R) - \nabla_{\mu}\nabla_{\nu}F(R) = 0$$
 (8)

which contains only the curvature tensor and F(R) in (7). The solution of this equation (black hole solution, actually) directly involves the Symmergent gravity parameters G and c_0 , and gains, therefore, direct dependence on the QFT properties via the defining equations (2) and (3).

Now, we give static black hole solution of the f(R) gravity equations in (8) as a simple illustration. To this end, we use the ansatz

$$F[R(r)] = \hat{\alpha} + br \tag{9}$$

in spherical coordinates $x^{\alpha} = \{t, r, \theta, \phi\}$ appropriate for black hole spacetime. The metric takes the form

$$ds^{2} = -f(r)dt^{2} + \frac{1}{f(r)}dr^{2} + r^{2}\left(d\theta^{2} + \sin^{2}\theta d\phi^{2}\right),$$
(10)

with the lapse function

$$f(r) = 1 - \frac{2GM}{r} - \frac{1 - \hat{\alpha}}{24\pi Gc_0} r^2 \tag{11}$$

approaching to the Schwarzschild black hole spacetime as $\hat{\alpha} \to 1$ or/and $c_0 \to \infty$. From now on, we set G = 1. In the next section, we analyze the rotating black hole solution in Symmergent gravity.

III. ROTATING BLACK HOLES IN SYMMERGENT GRAVITY

Appropriate for a rotating black hole geometry, we use the Boyer-Lindquist coordinates with a metric free of the coordinate singularities in the spacetime exterior to the black hole and interior to the cosmological horizon. The metric takes the form [97–102]

$$ds^{2} = \frac{\rho^{2}}{\Delta_{r}} dr^{2} + \frac{\rho^{2}}{\Delta_{\theta}} d\theta^{2} + \frac{\Delta_{\theta} \sin^{2} \theta}{\rho^{2}} \left[a dt - \left(r^{2} + a^{2} \right) \frac{d\phi}{\Xi} \right]^{2} - \frac{\Delta_{r}}{\rho^{2}} \left(dt - a \sin^{2} \theta \frac{d\phi}{\Xi} \right)^{2}$$

$$(12)$$

with the parameters

$$\Delta_r = (r^2 + a^2) \left(1 - \frac{r^2}{3} \frac{(1 - \hat{\alpha})}{8\pi c_0} \right) - 2Mr,$$
(13)

$$\rho^2 = r^2 + a^2 \cos^2 \theta \,, \tag{14}$$

$$\Delta_{\theta} = 1 + \frac{r^2}{3} \frac{(1 - \hat{\alpha})}{8\pi c_0} a^2 \cos^2 \theta , \qquad (15)$$

$$\Xi = 1 + \frac{r^2}{3} \frac{(1 - \hat{\alpha})}{8\pi c_0} a^2 \,. \tag{16}$$

Here, a is the black hole spin parameter, and $\hat{\alpha}$ and c_O are the parameters of the Symmergent gravity.

The physical energy E and angular momentum J of the black hole are related to the parameters m and a via the relations [103, 104]

$$E = \frac{m}{\Xi^2}, \quad J = \frac{am}{\Xi^2} \tag{17}$$

in which m is determined by solving the equation $\Delta_r\left(r_+\right)=0$, with r_+ standing for the radius of the event horizon. In this way, one can express energy and angular momentum in terms of the parameters r_+ , a, and G. (One here notes that $\frac{1}{l^2}=\frac{(\hat{a}-1)}{24\pi G_N\,c_0}$, where the curvature radius l is related to the negative cosmological constant as $\Lambda=-3l^{-2}$). As a result, one finds

$$E = \frac{1}{2\Xi^2 r_+} \left(r_+^2 + a^2 + \frac{r_+^4}{l^2} + \frac{a^2 r_+^2}{l^2} \right), \quad J = \frac{a}{2\Xi^2 r_+} \left(r_+^2 + a^2 + \frac{r_+^4}{l^2} + \frac{a^2 r_+^2}{l^2} \right). \tag{18}$$

as the explicit expressions for the definitions in (17).

Numerically, horizons can be determined by analyzing the lapse function, that is, by solving $\Delta_r=0$ using its definition in (13). Besides, the location of the ergoregions can be determined numerically by plotting the metric component g_{tt} and looking for points satisfying $g_{tt}=0$. In fact, plotted in Fig. 1 are Δ_r and $g_t t$ as functions of r for the integration constant $\hat{\alpha}=0.9$, black hole spin parameter a=0.9 M, and the various values of c_O . Here and onwards, one notes that depending on the sign of c_O , the Symmergent black hole mimics the dS ($c_O>0$) or AdS-Kerr ($c_O<0$) black holes. One also notes that the dS-Kerr black hole is obtained by replacing l^2 should be replaced by $-l^2$ in the AdS-Kerr black hole. It is worth noting that one gets AdS-Kerr black hole from the dS-Kerr black hole simply by changing the signs of $\hat{\alpha}$ or c_O .

Usually, the value of the cosmological constant is scaled to a higher value to see its overall effect. Thus, the assumed values of $\hat{\alpha}$ and $c_{\rm O}$ also follow the same reasoning. As we can see, the null boundaries are greatly affected by the choices for the parameters $\hat{\alpha}$ and $c_{\rm O}$. We can see that $c_{\rm O}>0$ produces three horizons, where, in the context of dS spacetime, the third horizon represents the cosmic outer boundary. The two other null boundaries are known as the Cauchy and event horizons. The Symmergent AdS solution, however, gives only two horizons. The Symmergent gravity effects are almost vanishingly small on the inner horizon compared to the outer horizon. As for the ergoregions, $c_{\rm O}>0$ leads to three ergoregions, and it can be seen that the farthest one turns out to be even beyond the cosmic horizon.

The Hawking temperature is given by

$$T = \frac{\kappa}{2\pi} \tag{19}$$

in which κ is the surface gravity defined as

$$\kappa^2 = -\frac{1}{2} \nabla^\mu \chi^\nu \nabla_\mu \chi_\nu \tag{20}$$

in terms of the null Killing vectors χ^{ν} . The metric has the Killing vectors $\xi^{\nu} = \partial_t$ and $\zeta^{\nu} = \partial_{\varphi}$ that are associated with the time translation and rotational invariance, respectively. Consequently, we take

$$\chi^{\nu} = \xi^{\nu} + \Omega \zeta^{\nu} \tag{21}$$

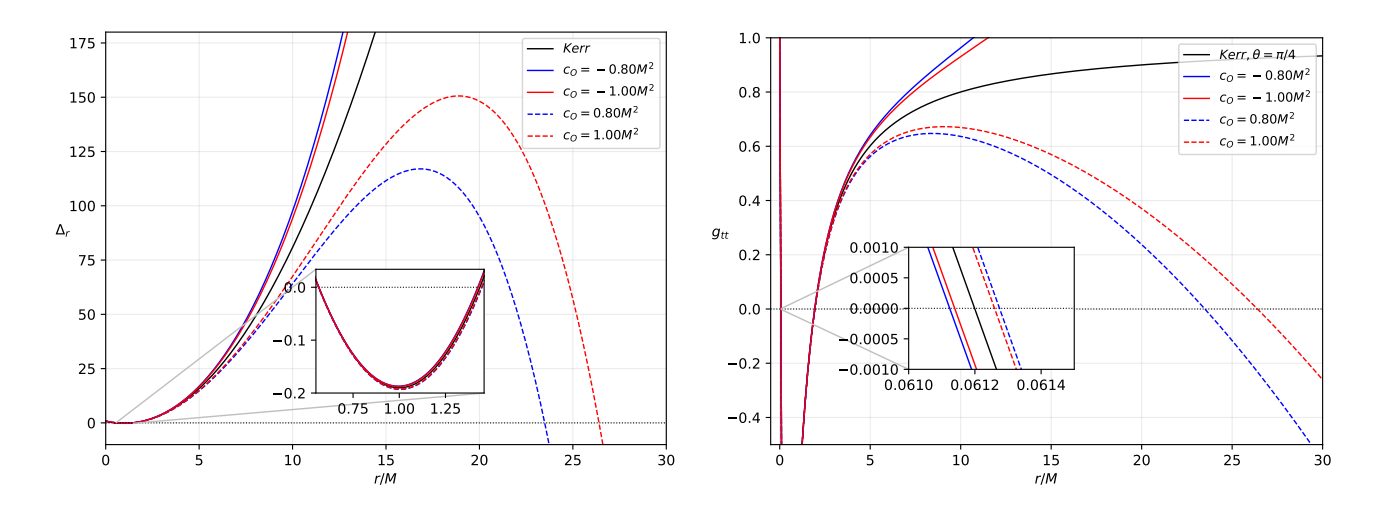


FIG. 1. The plots of the functions Δ_r (left window) and g_{tt} (right-window) as functions of r for the integration constant $\hat{\alpha}=0.9$, black hole spin parameter a=0.9 M, and the various values of c_O . The right-window shows the location of the ergoregion for $\theta=\pi/4$.

and determine Ω under the condition that χ^{ν} is a null vector. The equation leads to

$$\chi^{\nu}\chi_{\nu} = g_{tt} + 2\Omega g_{t\varphi} + \Omega^2 g_{\varphi\varphi} = 0, \tag{22}$$

from which one gets

$$\Omega = -\frac{g_{t\varphi}}{g_{\varphi\varphi}} \pm \sqrt{\left(\frac{g_{t\varphi}}{g_{\varphi\varphi}}\right)^2 - \frac{g_{tt}}{g_{\varphi\varphi}}} \tag{23}$$

which reduces to

$$\Omega_{+} = \frac{a\Xi}{r_{+}^{2} + a^{2}}.$$
 (24)

at the event horizon $\Delta(r_+) = 0$. This Ω value leads then to the surface gravity

$$\kappa = \frac{1}{2\left(r_+^2 + a^2\right)} \left. \frac{d\Delta_r}{dr} \right|_{r=r_+} \tag{25}$$

and the corresponding Hawking temperature

$$T = \frac{r_{+}}{4\pi \left(r_{+}^{2} + a^{2}\right)} \left(1 + \frac{a^{2}}{l^{2}} + \frac{3r_{+}^{2}}{l^{2}} - \frac{a^{2}}{r_{+}^{2}}\right)$$
(26)

which can be rewritten as

$$T = \frac{3r_{+}^{4} + (a^{2} + l^{2}) r_{+}^{2} - l^{2} a^{2}}{4\pi l^{2} r_{+} (r_{+}^{2} + a^{2})}.$$
 (27)

The Bekenstein-Hawking entropy is given by

$$S = \frac{A}{4} = \frac{\pi \left(r_{+}^{2} + a^{2}\right)}{\Xi} \tag{28}$$

where all thermodynamic quantities must be non-negative. The rotating Symmergent black hole satisfies, therefore the first law of thermodynamics

$$dE = TdS + \Omega dJ \tag{29}$$

with

$$\Omega = \frac{a\left(1 + r_{+}^{2}l^{-2}\right)}{r_{+}^{2} + a^{2}}.$$
(30)

IV. GEODESICS ROTATING SYMMERGENT BLACK HOLES

A. Null geodesic and shadow cast

In this section, we first begin with the study of null geodesics. To begin, the Hamilton-Jacobi states that

$$\frac{\partial S}{\partial \lambda} = -H,\tag{31}$$

where S is the Jacobi action in terms of the affine parameter λ and coordinates x^{μ} . In GR, the Hamiltonian is known to take the form

$$H = \frac{1}{2}g^{\mu\nu}\frac{\partial S}{\partial x^{\mu}}\frac{\partial S}{\partial x^{\nu}},\tag{32}$$

and using Eq. (31), it follows that

$$\frac{\partial S}{\partial \lambda} = -\frac{1}{2} g^{\mu\nu} \frac{\partial S}{\partial x^{\mu}} \frac{\partial S}{\partial x^{\nu}}.$$
 (33)

Using the separability anzats, where μ is the particle's rest mass,

$$S = \frac{1}{2}\mu^2\lambda - Et + L\phi + S_r(r) + S_\theta(\theta)$$
(34)

due to the variable coordinate independence in t, ϕ , and λ , the following equations of motion can be derived in its first-order form [105]:

$$\Sigma \frac{dt}{d\lambda} = \frac{\Xi(r^2 + a^2)P(r)}{\Delta_r} - \frac{\Xi aP(\theta)}{\Delta_{\theta}},$$

$$\Sigma \frac{dr}{d\lambda} = \sqrt{R(r)},$$

$$\Sigma \frac{d\theta}{d\lambda} = \sqrt{\Theta(\theta)},$$

$$\Sigma \frac{d\phi}{d\lambda} = \frac{\Xi aP(r)}{\Delta_r} - \frac{\Xi P(\theta)}{\Delta_{\theta} \sin^2 \theta},$$
(35)

where

$$R(r) = P(r)^{2} - \Delta_{r}(\mu^{2}r^{2} + K)$$

$$P(r) = \Xi E(r^{2} + a^{2}) - \Xi aL$$

$$\Theta(\theta) = \Delta_{\theta}(K - \mu^{2}a^{2}\cos^{2}\theta) - \frac{P(\theta)^{2}}{\sin^{2}\theta}$$

$$P(\theta) = \Xi(aE\sin^{2}\theta - L)$$
(36)

From the third equation in Eq. (35), the constants of motion can then be connected by the relation $K = \Xi^2(aE - L)^2$, which is a consequence of a hidden symmetry in the θ -coordinate, found by Carter [105, 106].

First, we study null geodesic and shadow cast by setting $\mu = 0$. Photon circular orbits, which are always unstable, must satisfy the following conditions:

$$R(r) = \frac{dR(r)}{dr} \mid_{r=r_0} = 0.$$
 (37)

This section will discuss the shadow cast by a rotating Symmergent black hole, where the null geodesic is important. In particular, we need the photon region in constant r_0 , called the photonsphere, which is an unstable orbit. The shadow cast ultimately depends on such a photon region. With $\mu=0$, it is convenient to define the following impact parameters:

$$\xi = \frac{L}{E}, \quad \eta = \frac{K}{E^2}. \tag{38}$$

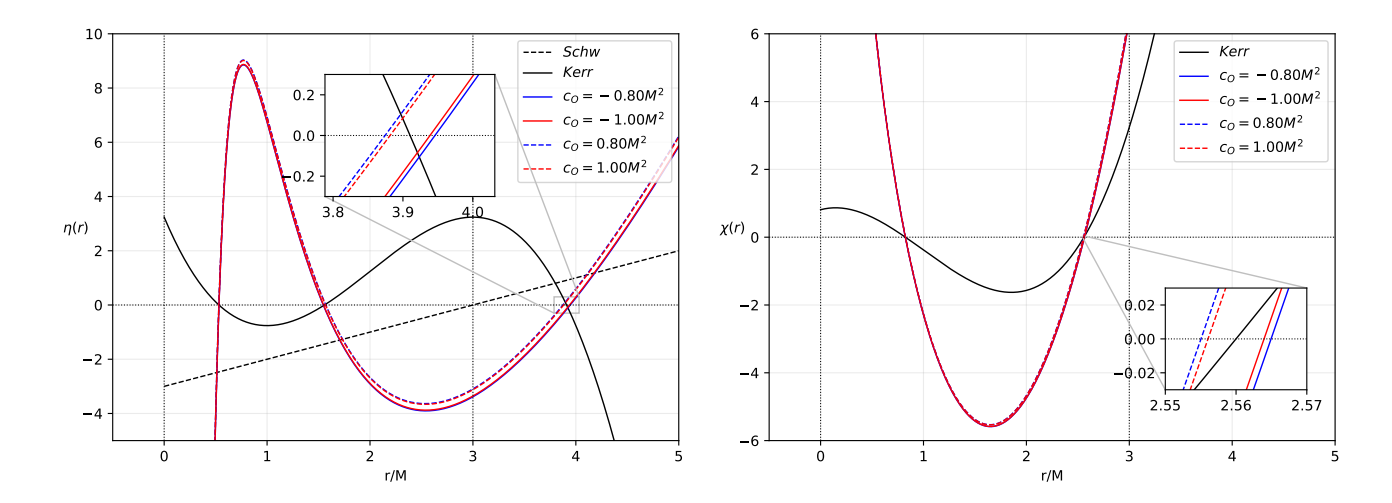


FIG. 2. Location of photonsphere (left). Location of photonsphere crossing at $\phi = 0$ or along the equatorial plane (right). In this plot, the constant of integration is $\hat{a} = 0.90$, and the spin parameter is a = 0.90M

After some considerable algebra, we find the following equations:

$$\xi = \frac{\Delta_r'(r^2 + a^2) - 4\Delta_r r}{a\Delta_r'},\tag{39}$$

$$\eta = \frac{-r^4 \Delta_r'^2 + 8r^3 \Delta_r \Delta_r' + 16r^2 \Delta_r (a^2 - \Delta_r)}{a^2 \Delta_r'^2}.$$
(40)

The photonsphere radius $r_{\rm ph}$ can then be found by solving r when $\eta(r)=0$. The analytical solutions are well-known for both Schwarzschild and Kerr black holes. In our case, we plot the Eq. (40) to obtain qualitative impression about the location of $r_{\rm ph}$. The left figure considers the location of the photonsphere along the equatorial plane. As we would expect, the Schwarzschild case gives $r_{ph}=3M$. The extreme Kerr case gives two possible locations for the photonsphere: the prograde orbit is $r_{ph}=M$, while the retrograde orbit is $r_{ph}=4M$. The plot shows the locations for a=0.90M, which are near the said extreme values. For the Symmergent effect, the dS type gives slightly lower values in the retrograde case, while the AdS type gives a higher one (see inset plot). The Symmergent effect is also present in the prograde case. While a similar effect occurs, the deviation is smaller than in the retrograde case. In the right figure, we also considered photons with zero angular momentum, that is, those that traverse the equatorial plane in a perpendicular manner (called nodes). The retrograde case gives higher values for such an orbit than the prograde case. The deviation caused is nearly not evident, especially in the prograde case. However, we can still see deviation when we zoom in on the retrograde case when similar effects can be said before. As a final remark, note that the Symmergent effect behaves like a dS or AdS case, where such behavior is not present in the Schwarzschild case. The coupling between the spin and Symmergent parameters made it possible to influence the behavior of the photonsphere.

Escaping photons in the unstable orbit gives the possibility for remote observers to backward trace and obtain a shadow cast by using the celestial coordinates $(r_{\text{obs}}, \theta_{\text{obs}})$. Such an observer is also known as the Zero Angular Momentum Observer (ZAMO). Also, in this type of co-moving frame, the approximation $r_{\text{obs}} \to \infty$ is implemented, and $\theta_{\text{obs}} = \pi/2$ is assumed without compromising generality. The celestial coordinates are defined as [107]

$$\alpha = -r_{\text{obs}} \frac{\xi}{\zeta \sqrt{g_{\phi\phi}} \left(1 + \frac{g_{t\phi}}{g_{\phi\phi}} \xi\right)},$$

$$\beta = r_{\text{obs}} \frac{\pm \sqrt{\Theta(i)}}{\zeta \sqrt{g_{\theta\theta}} \left(1 + \frac{g_{t\phi}}{g_{\phi\phi}} \xi\right)},$$
(41)

and the condition $r_{\rm obs} o \infty$ simplifies these as

$$\alpha = -\xi \csc \theta_{\text{obs}},$$

$$\beta = \pm \sqrt{\eta + a^2 \cos^2 \theta_{\text{obs}} - \xi^2 \cot^2 \theta_{\text{obs}}}.$$
(42)

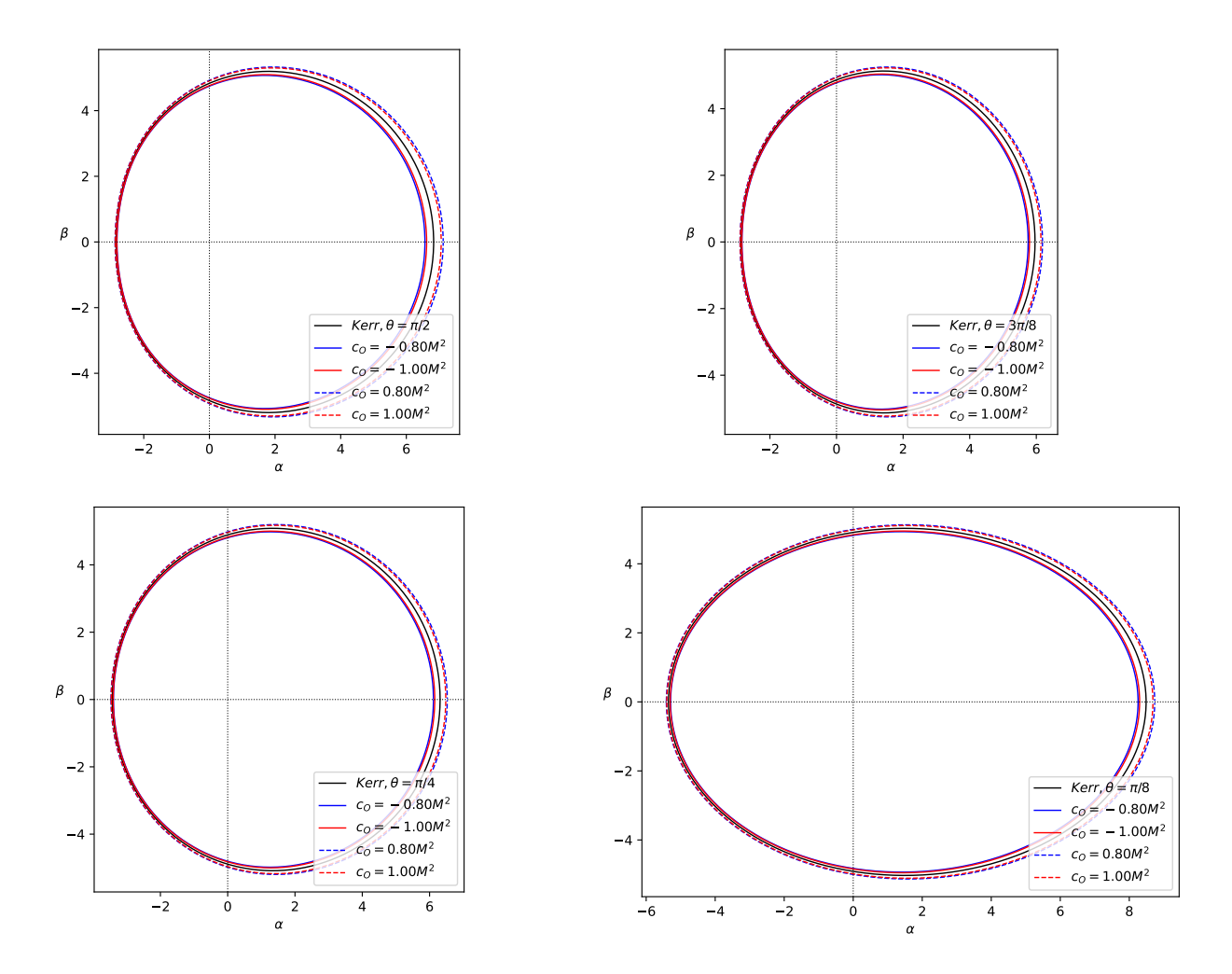


FIG. 3. Shadow plot for different inclination angles. The spin parameter is chosen to be a=0.90M, and $\hat{a}=0.90$. The aspect ratio of the plot is set to equal to obtain the actual view.

Note how the above expressions simplify further when $\theta_{\rm obs}=\pi/2$, and if a=0, the shadow cast of a Schwarzschild black hole as a circle can be obtained. The plot of β vs. α is shown in Fig. 3 as we fixed the rotation parameter to a=0.90M. Overall, we can see the D-shaped Nature of the shadow due to the spin parameter. Commenting first on the effect of the inclination angle, we see that as we decrease the value of θ (going up from the equatorial plane), we can see the shape varies. Remarkably, in the upper right figure, the shape becomes more compressed in the x-axis, and as one continues to go up (lower left figure), it turns back to an almost spherical shape. Finally, near the pole, a drastic change in the shadow shape occurs due to stretching the x-axis. For the Symmergent effect, note that the dS type tends to decrease the photonsphere radius. Nevertheless, as photons travel in the intervening space affected by the Symmergent parameter, the shadow size is seen to increase. We can see the same thing in the AdS type Symmergent effect; whereas the photonsphere increases, the reverse happens to the shadow size.

In the azimuthal plane, we see how the shadow becomes "D-shaped" when a is near extremal. The numerical value of the shadow radius associated with this shape [44, 65], can be calculated [45] using

$$R_{\rm s} = \frac{\beta_{\rm t}^2 + (\alpha_{\rm t} - \alpha_{\rm r})^2}{2|\alpha_{\rm t} - \alpha_{\rm r}|}.$$
(43)

We plot this equation in Fig. 4 (upper left), along with the shadow's angular radius (upper right) defined by

$$\theta_{\rm sh} = 9.87098 \times 10^{-3} \frac{R_{\rm s} M}{D}, \text{ and.}$$
 (44)

In using Eq. (44), the mass M of the black hole should be in terms of M_{\odot} , and D is in parsec. Note that these visualizations are consistent with Fig. 3. Other observables that can be derived from the shadow are the distortion parameter and the energy

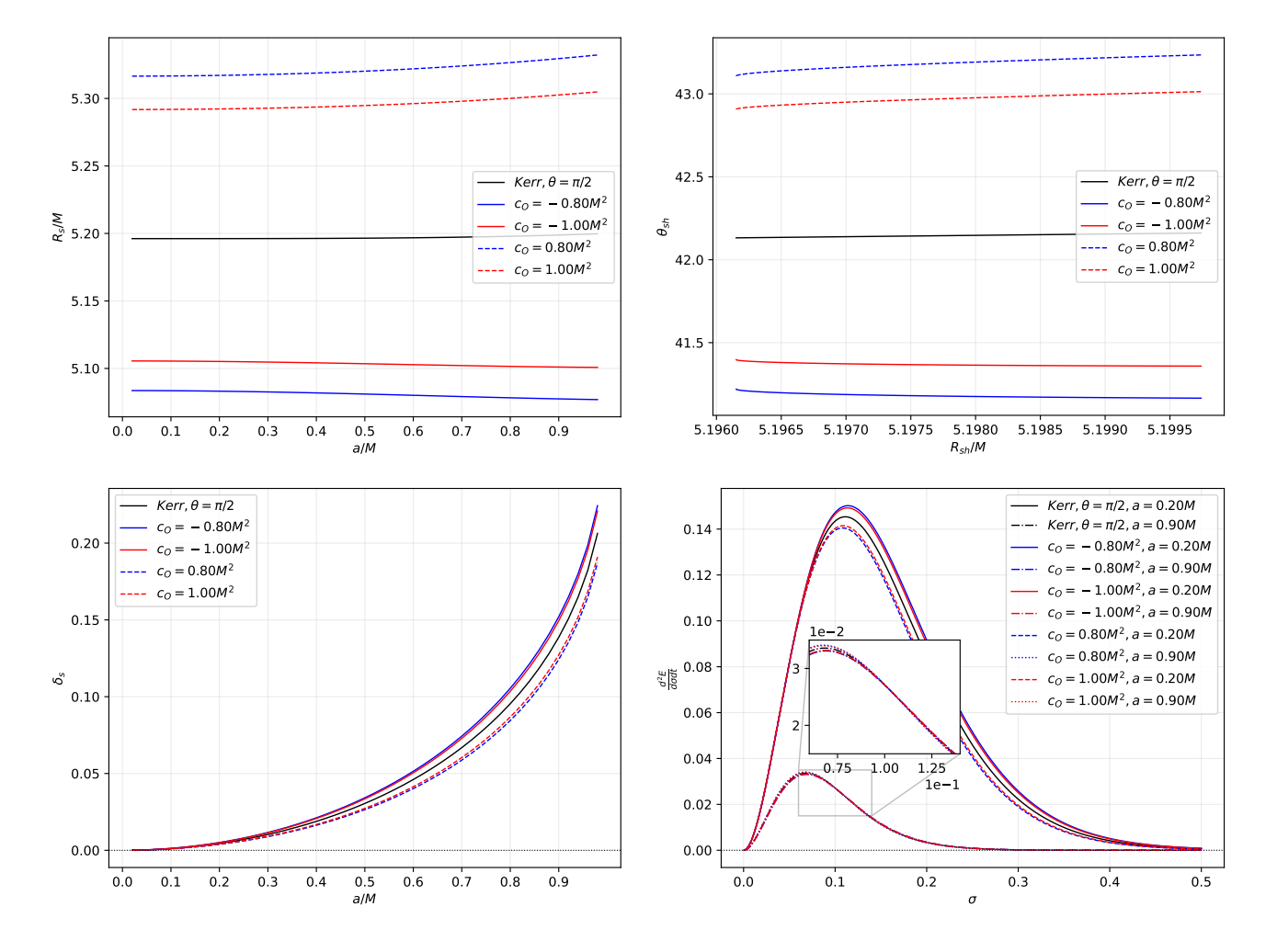


FIG. 4. Shadow observables associated with the upper left figure in Fig. 3. Upper left: Shadow radius, upper right: angular diameter (in μ as) for M87*, lower left: distortion parameter, lower right: energy emission rate.

emission rate, defined via

$$\delta_{\rm s} = \frac{d_{\rm s}}{R_{\rm s}} = \frac{\tilde{\alpha}_{\rm l} - \alpha_{\rm l}}{R_{\rm s}},\tag{45}$$

$$\frac{d^2E}{d\omega dt} = 2\pi^2 \frac{\Pi_{ilm}}{e^{\omega/T} - 1} \omega^3 \tag{46}$$

respectively. We can see how the spin parameter affects the distortion of the shadow, that is, to increase its value. We can also observe that even if the dS Symmergent effect tends to increase the shadow, the distortion it gives is smaller than the AdS Symmergent effect. For Eq. (46), the energy absorption cross-section $\Pi_{ilm} \sim \pi R_{\rm s}^2$ can be approximated for an observer at $r_{\rm obs} \to \infty$. The Hawking temperature T due to a rotating black hole is given in Eq. 27 can be calculated as follows:

$$T = \frac{r_{\rm h}}{4\pi(r_{\rm h}^2 + a^2)^2} \left[2a^2(f(r_{\rm h}) - 1) + r_{\rm h}(r_{\rm h}^2 + a^2)f'(r_{\rm h}) \right],\tag{47}$$

where r_h is the radius of the event horizon, and $f(r_h) = g_{tt}$. We plot these observables in Fig. 4. In the lower right figure of Fig. 4, we can see the comparison between a = 0.20M and a = 0.90M for the Kerr, dS, and AdS Symmergent cases. The energy emission rate is strongest while having a larger value for peak frequency for lower values of a. Now, observing the inset plot, we can say that the dS and AdS Symmergent effects have opposite effects between a = 0.20M and a = 0.90M. In particular, when a = 0.20M, AdS type increases the energy emission rate further, at a = 0.90M, it tends to decrease it further. The same observation can be noted with the dS type but with the opposite effect.

Black hole	Mass (M_{\odot})	Angular diameter: $2\theta_{\rm sh}$ (μ as)	Distance (kpc)
Sgr. A*	4.3 ± 0.013 x 10^{6} (VLTI)	$48.7 \pm 7 (\text{EHT})$	8.277 ± 0.033
M87*	$6.5 \pm 0.90 \text{x} 10^9$	$ 42 \pm 3 $	16800

TABLE I. Black hole observational constraints.

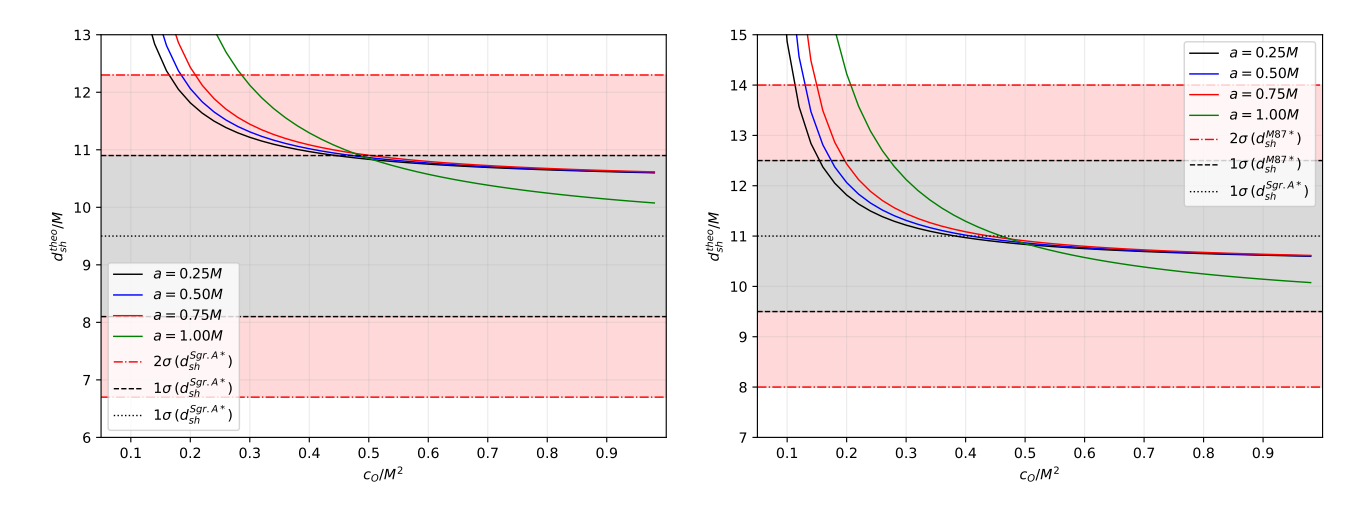


FIG. 5. Sgr. A*(left), M87*(right). Both are plotted assuming that one of the Symmergent parameters is $\hat{\alpha} = 0.90$.

Let us now discuss the observational constraint of the Symmergent parameter c_0 using the obtained data from M87* [108] and Sgr. A* [96] in relation to black hole shadow. These important observational data are in Table I. With these data, one can find the diameter of the shadow size in units of the black hole mass with

$$d_{\rm sh} = \frac{D\theta}{M}.\tag{48}$$

Thus, the diameter of the shadow image of M87* and Sgr. A* are $d_{\rm sh}^{\rm M87*}=(11\pm1.5)m$, and $d_{\rm sh}^{\rm Sgr.~A*}=(9.5\pm1.4)m$ respectively. Meanwhile, the theoretical shadow diameter can be obtained via $d_{\rm sh}^{\rm theo}=2R_{\rm sh}$ where we used Eq. (43). Based on Fig. 5, we can conclude that the parameters we used in describing the shadow cast fall within the upper and lower bounds of 1σ level. Where this happens, the range in c_0 is more extensive in M87* than in Sgr. A*.

	Sgr. A*	2σ		1σ		observed $R_{\rm sh}$
	spin a	upper	lower	upper	lower	mean
	0.25M	0.165	-	0.445	-	-
ĺ	0.50M	0.185	-	0.471	-	-
ı	0.75M	0.209	-	0.504	-	-
	M	0.287	-	0.486	-	-

M87*	2σ		1σ		observed $R_{ m sh}$
spin a	upper	lower	upper	lower	mean
0.25M	0.113	-	0.155	-	0.383
0.50M	0.130	-	0.174	-	0.409
0.75M	0.150	-	0.197	-	0.440
M	0.207	-	0.273	-	0.460

TABLE II. Values of c_0 as generated in Fig. 5.

B. Symmergent effects on time-like orbits: Effective potential and ISCO radii

Let us now turn our attention to time-like orbits. Here, we will still use the equations of motion from the Hamilton-Jacobi approach and set $\mu=1$ to study time-like orbits. We are interested in determining the location of the ISCO radius, which is very important in the study of matter accretion disks, and the effective potential to get a qualitative description of bound and unbound orbits under the Symmergent effects.

To obtain some qualitative behavior of the massive particle's motion around the Symmergent black hole (i.e., bound, stable, and unstable circular orbits), we use the effective potential formula [109], which, in terms of the inverse metric,

$$V_{\pm} = \frac{g^{t\phi}}{g^{tt}} L \pm \left\{ \left[\left(\frac{g^{t\phi}}{g^{tt}} \right)^2 - \frac{g^{\phi\phi}}{g^{tt}} \right] L^2 - \frac{1}{g^{tt}} \right\}^{1/2}. \tag{49}$$

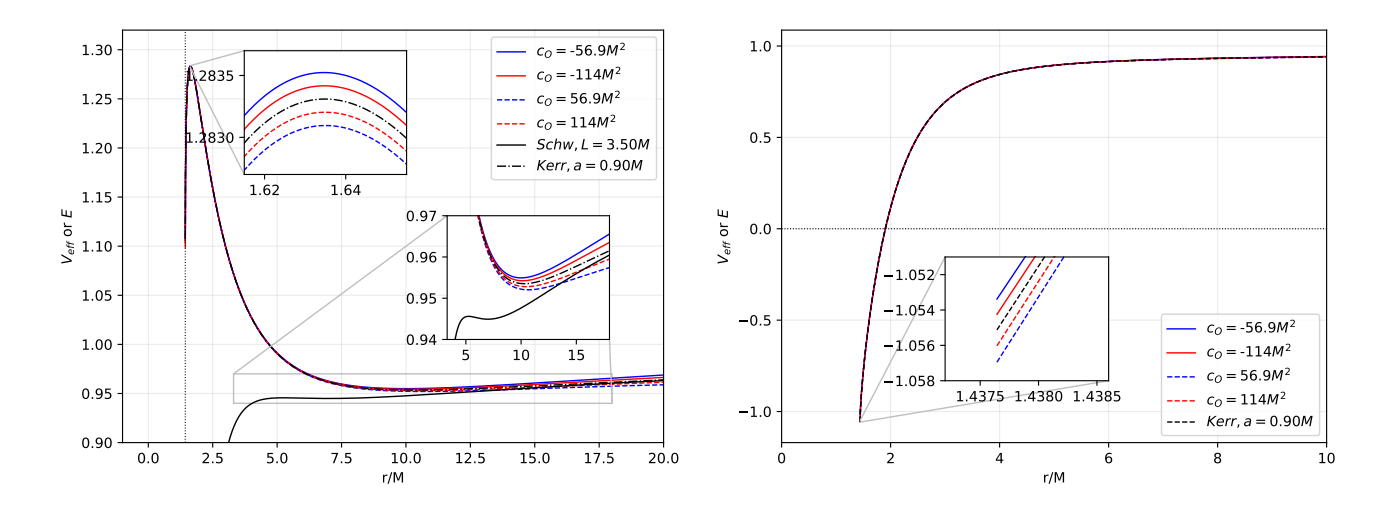


FIG. 6. Plot of the effective potential. The left figure indicates +L, while the right for -L. a=0.90M is used, and $\hat{\alpha}=0.90$.

The plot for $L=\pm 3.50M$ is shown in Fig. 6. In this figure, maxima and minima represent the unstable and stable circular orbits, respectively. We remark that for the a=0 (Schwarzschild) case, the maxima of the effective potential curve are way lower compared when a=0.90M (Kerr case). The Symmergent parameters are chosen to see some noticeable deviation from the Kerr case with physical meaning. In the upper inset plot, we can see that the energy for an unstable circular orbit is higher in the AdS Symmergent effect than in the dS type. For a lower range of particle's energy, the radius of the stable circular orbit is smaller in the AdS type than the dS type. Same observation for the bound elliptical orbits. We also plotted the situation where the particle attains a negative angular momentum. It is known that it did not happen in the Schwarzschild case. As we can see in the right figure, particles with negative energies can be created near the rotating black hole's event horizon. Clearly, Symmergent affects the particle's energy magnitude, which contributes to the Penrose process and black hole evaporation.

In locating the ISCO radius, we use Eq. (37) and solve for the energy $E_{\rm cir}$. Assigning $X^2 = L - aE$ [105, 110],

$$X^{2} = \frac{r^{3} \left(\Delta_{r}^{\prime} - 2E_{\text{cir}}^{2} r\right)}{-2a^{2} - r\Delta_{r}^{\prime} + 2\Delta_{r}}.$$
 (50)

We differentiate again Eq. (50) with respect to r since $E_{cir} = E_{isco}$. After some algebra,

$$E_{\rm isco}^2 = \frac{1}{Br} \left\{ a^2 \left[-\left(r\Delta_r'' + 3\Delta_r'\right) \right] + r\Delta_r \Delta_r'' - 2r\Delta_r'^2 + 3\Delta_r \Delta_r' \right\},\tag{51}$$

where $B = -8a^2 + r(r\Delta_r'' - 5\Delta_r') + 8\Delta_r$. The ISCO radius can then be found via [44]

$$\eta(r)_{\text{isco}} = \pm 2\Delta_r \left(a^2 - \Delta_r\right)^2 \pm \frac{9}{4} r \Delta_r \left(a^2 - \Delta_r\right) \Delta_r' \pm \frac{1}{16} r^3 \Delta_r' \left(\Delta_r \Delta_r'' - 2\Delta_r'^2\right)
\pm \frac{1}{16} r^2 \left[4\Delta_r \left(a^2 - \Delta_r\right) \Delta_r'' + \left(15\Delta_r - 4a^2\right) \Delta_r'^2\right]
+ a\Delta_r \sqrt{4a^2 + 2r\Delta_r' - 4\Delta_r} \left[-a^2 + \frac{1}{8} r \left(r\Delta_r'' - 5\Delta_r'\right) + \Delta_r\right] = 0.$$
(52)

Note that this reduces to the Kerr case when if $\Delta(r) = r^2 - 2mr + a^2$:

$$3a^2 \mp 8a\sqrt{m}\sqrt{r} + r(6m - r) = 0 \tag{53}$$

The upper and lower signs in Eq. (52) reveal the prograde and retrograde orbit of the massive particle in the ISCO radius, respectively. We numerically plot Eq. (52) shown in Fig. 7. First, let us note that in the Schwarzschild case, the ISCO radius is located at r = 6M. For an extreme Kerr case, the prograde ISCO is at r = M (which coincides with the prograde photonsphere), while retrograde ISCO is at r = 9M. Thus, the right figure represents the retrograde one where we can see clearly how the Symmergent parameters affect the radius. The innermost radius, which determines the accretion disk's innermost region, is smaller in the AdS type, while the dS type is slightly larger in the Kerr case. We note that the first root of η_{isco} is unphysical since those radii are smaller than the photonsphere in the retrograde case. Finally, we see the same Symmergent effects in the prograde ISCO. To close this section, we remark that the combination of Symmergent parameters for the time-like particles produces weak

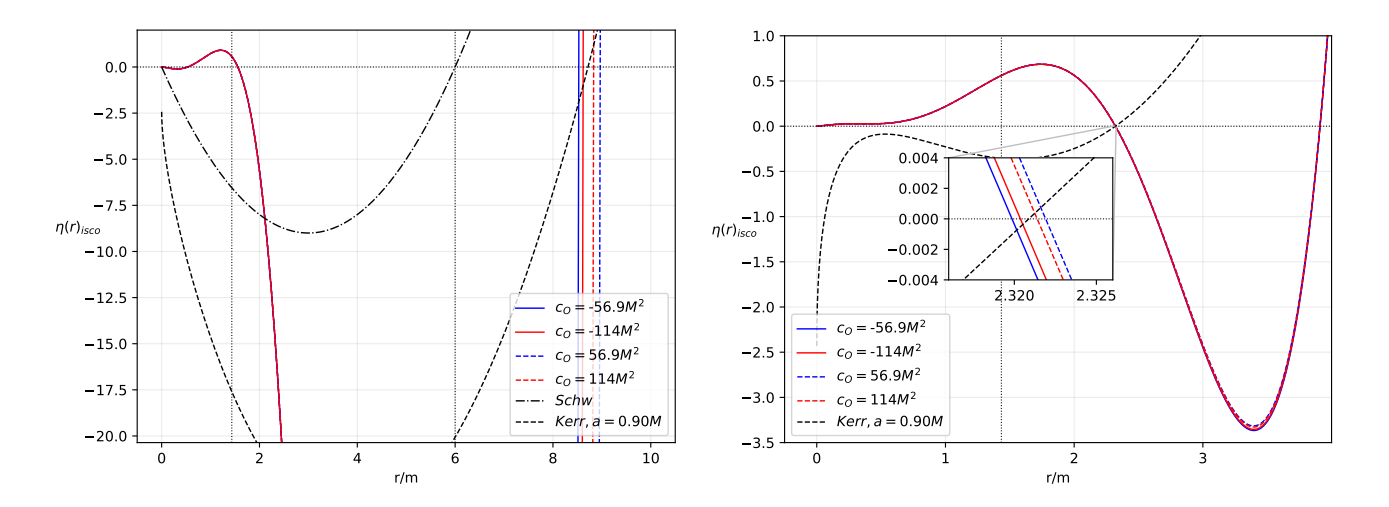


FIG. 7. Location of ISCO. Left: counter-rotation of a massive particle, right: co-rotation of a massive particle. a=0.90M is used, and $\hat{\alpha}=0.90$.

Symmergent effects than the null particles such as photons. In other words, if these parameters are used in null particles, we can see negligible Symmergent effects. We then conclude that time-like particles are more sensitive to Symmergent effects than the null particles.

V. WEAK DEFLECTION ANGLE BY ROTATING SYMMERGENT BLACK HOLES USING GAUSS-BONNET THEOREM

This section investigates the deflection angle of light rays around the rotating Symmergent black hole in the weak field limit using the method defined in [32, 34]. Now, let us briefly summarize the formalism of the finite distance method.

First, we define the deflection angle as follows:

$$\Theta = \Psi_{R} - \Psi_{S} + \phi_{SR} \tag{54}$$

. It is noted that ϕ_{SR} is the longitude separation angle, Ψ_R , and Ψ_S stands for the angles between the light rays and the radial direction at the observer and the source position, respectively. Unit tangential vector e^i is used to write the above angle as follows:

$$(e^r, e^\theta, e^\phi) = \epsilon \left(\frac{dr}{d\phi}, 0, 1\right) \tag{55}$$

here, ϵ is a radial quantity. One can write the stationary spacetime in this form:

$$ds^{2} = -A(r,\theta)dt^{2} + B(r,\theta)dr^{2} + C(r,\theta)d\theta^{2} + D(r,\theta)d\phi^{2} - 2H(r,\theta)dtd\phi,$$
(56)

then, it is straightforward to calculate the ϵ :

$$\epsilon = \frac{A(r)D(r) + H^{2}(r)}{A(r)(H(r) + A(r)b)},$$
(57)

where b is the impact parameter. We can write the conserved quantities: energy and the angular momentum

$$E = A(r)\dot{t} + H(r)\dot{\phi} \qquad L = D(r)\dot{\phi} - H(r)\dot{t}. \tag{58}$$

Using the equatorial plane $(\theta = \frac{\pi}{2})$, the line element reduces to

$$dl^2 \equiv \gamma_{ij} dx^i dx^j \tag{59}$$

with a spatial metric γ_{ij} and defining the angle as

$$\cos \Psi \equiv \gamma_{ij} e^i R^j. \tag{60}$$

Note that R^j are the components of a radial vector given by $(\frac{1}{\sqrt{\gamma_{rr}}}, 0, 0)$. Then we use the Eq.(55) and Eq.(60), to obtain the $\sin \Psi$ term:

$$\sin \Psi = \frac{H(r) + A(r)b}{\sqrt{A(r)D(r) + H^2(r)}}.$$
(61)

Now we can calculate the deflection angle of the Symmergent black hole in the weak field limit using the method. First, we use the impact parameter given by $b=\frac{L}{E}$ and changing the variable r to $\frac{1}{u}$, we can get

$$\left(\frac{du}{d\phi}\right)^{2} = \frac{1}{b^{2}} - \frac{4aMu}{b^{3}} - u^{2} + 2Mu^{3} + \frac{1-\hat{\alpha}}{24\pi c_{0}} - \frac{2a}{3b^{3}u^{2}} \frac{(1-\hat{\alpha})}{8\pi c_{0}} - \frac{8aM}{3b^{3}u} \frac{(1-\hat{\alpha})}{8\pi c_{0}} + \mathcal{O}\left[M^{2}, \left(\frac{1-\hat{\alpha}}{8\pi c_{0}}\right)^{2}, a^{2}\right], \quad (62)$$

where one has considered only the retrograde solution. In the beginning, one should calculate the separation angle integral. Putting $\left(\frac{du}{d\phi}\right)^2 = F(u)$, this can be determined via the following computation

$$\phi_{RS} = \int_{S}^{R} d\phi = \int_{u_{S}}^{u_{0}} \frac{1}{\sqrt{F(u)}} du + \int_{u_{R}}^{u_{0}} \frac{1}{\sqrt{F(u)}} du, \tag{63}$$

where u_S and u_R are the inverse of the source and the observer distance from the black hole and where u_0 is the inverse of the closest approach r_0 . Considering the weak field and the slow rotation approximations, the impact parameter can be related to u_0 as follows

$$b = \frac{1}{u_0} + M - 2aMu_0 + \mathcal{O}\left[M^2, \left(\frac{1-\hat{\alpha}}{8\pi c_0}\right)^2, a^2\right].$$
 (64)

Performing appropriate calculations, we obtain

$$\phi_{RS} = \phi_{RS}^{Kerr} + \left(\frac{u_{R}}{\sqrt{1 - b^{2}u_{R}^{2}}} + \frac{u_{S}}{\sqrt{1 - b^{2}u_{S}^{2}}}\right) \frac{b^{3}}{6} \frac{(1 - \hat{\alpha})}{8\pi c_{O}} + \left(\frac{b\left(2 - 3b^{2}u_{R}^{2}\right)}{2\left(1 - b^{2}u_{R}^{2}\right)^{3/2}} + \frac{b\left(2 - 3b^{2}u_{S}^{2}\right)}{2\left(1 - b^{2}u_{S}^{2}\right)^{3/2}}\right) \frac{M}{3} \frac{(1 - \hat{\alpha})}{8\pi c_{O}} + \left(\frac{1 - 2b^{2}u_{R}^{2}}{u_{R}\sqrt{1 - b^{2}u_{R}^{2}}} + \frac{1 - 2b^{2}u_{S}^{2}}{u_{S}\sqrt{1 - b^{2}u_{S}^{2}}}\right) \frac{a}{3} \frac{(1 - \hat{\alpha})}{8\pi c_{O}} + \mathcal{O}\left[M^{2}, \left(\frac{1 - \hat{\alpha}}{8\pi c_{O}}\right)^{2}, a^{2}\right], \tag{65}$$

where the Kerr term is given by

$$\phi_{\text{RS}}^{\text{Kerr}} = \phi_{\text{RS}}^{\text{SW}} - \left(\frac{1}{\sqrt{1 - b^2 u_{\text{R}}^2}} + \frac{1}{\sqrt{1 - b^2 u_{\text{S}}^2}}\right) \frac{2aM}{b^2}.$$
 (66)

In this equation, the Schwarzschild term is

$$\phi_{\text{RS}}^{\text{Schw}} = \pi - \arcsin(bu_{\text{R}}) - \arcsin(bu_{\text{S}}) + \left(\frac{2 - b^2 u_{\text{R}}^2}{\sqrt{1 - b^2 u_{\text{R}}^2}} + \frac{2 - b^2 u_{\text{S}}^2}{\sqrt{1 - b^2 u_{\text{S}}^2}}\right) \frac{M}{b}.$$
 (67)

To get the remaining terms appearing in the light deflection angle expression, one should identify the Ψ terms. We find

$$\sin \Psi = bu - bMu^2 + 2aMu^2 - \left(\frac{bM}{6} - \frac{a}{3u} + \frac{b}{6u}\right) \frac{(1-\hat{\alpha})}{8\pi c_0} + \mathcal{O}\left[M^2, \left(\frac{1-\hat{\alpha}}{8\pi c_0}\right)^2, a^2\right].$$
 (68)

This relation produces

$$\begin{split} \Psi_{\mathrm{R}} - \Psi_{\mathrm{S}} &= \Psi_{\mathrm{R}}^{\mathrm{Kerr}} - \left(\frac{1}{u_{\mathrm{R}}\sqrt{1 - b^{2}u_{\mathrm{R}}^{2}}} + \frac{1}{u_{\mathrm{S}}\sqrt{1 - b^{2}u_{\mathrm{S}}^{2}}}\right) \frac{b}{6} \frac{(1 - \hat{\alpha})}{8\pi c_{\mathrm{O}}} - \left(\frac{2b^{2}u_{\mathrm{R}}^{2} - 1}{(1 - b^{2}u_{\mathrm{R}}^{2})^{3/2}} + \frac{2b^{2}u_{\mathrm{S}}^{2} - 1}{(1 - b^{2}u_{\mathrm{S}}^{2})^{3/2}}\right) \frac{bM}{6} \frac{(1 - \hat{\alpha})}{8\pi c_{\mathrm{O}}} \\ &+ \left(\frac{1}{u_{\mathrm{R}}\sqrt{1 - b^{2}u_{\mathrm{R}}^{2}}} + \frac{1}{u_{\mathrm{S}}\sqrt{1 - b^{2}u_{\mathrm{S}}^{2}}}\right) \frac{a}{3} \frac{(1 - \hat{\alpha})}{8\pi c_{\mathrm{O}}} + \mathcal{O}\left[M^{2}, \left(\frac{1 - \hat{\alpha}}{8\pi c_{\mathrm{O}}}\right)^{2}, a^{2}\right], \end{split}$$
(69)

where one has

$$\Psi_{\rm R}^{\rm Kerr} - \Psi_{\rm S}^{\rm Kerr} = \Psi_{\rm R}^{\rm Schw} - \Psi_{\rm R}^{\rm Schw} + \left(\frac{u_{\rm R}^2}{\sqrt{1 - b^2 u_{\rm R}^2}} + \frac{u_{\rm S}^2}{\sqrt{1 - b^2 u_{\rm S}^2}}\right) 2aM,\tag{70}$$

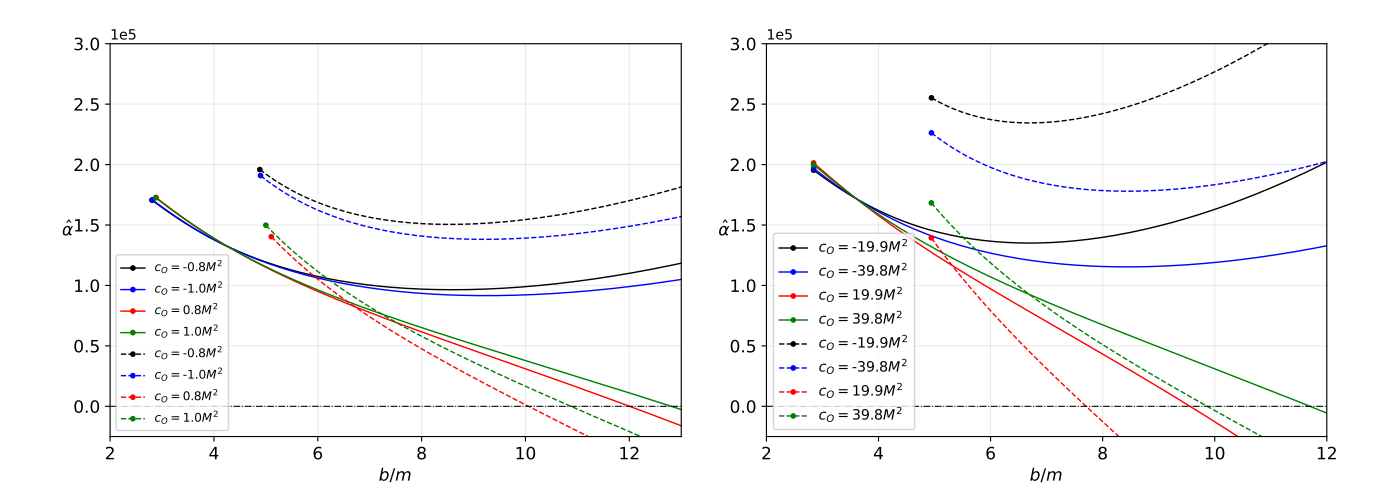


FIG. 8. Plot of the weak deflection angle of photons under the effect of the spin and Symmergent parameters a and c_0 and finite distance. The solid lines correspond to +a (prograde), while the dashed line corresponds to -a (retrograde). We assumed $u_S = u_R = 0.5b^{-1}$ (left), $u_S = u_R = 0.01b^{-1}$ (right), and $\hat{\alpha} = 0.90$. The dots represent the associated critical impact parameters in each case.

and where one has found

$$\Psi_{\rm R}^{\rm Schw} - \Psi_{\rm R}^{\rm Schw} = \left(\arcsin\left(bu_{\rm R}\right) + \arcsin\left(bu_{\rm S}\right) - \pi\right) - \left(\frac{u_{\rm R}^2}{\sqrt{1 - b^2 u_{\rm R}^2}} + \frac{u_{\rm S}^2}{\sqrt{1 - b^2 u_{\rm S}^2}}\right) Mb. \tag{71}$$

Combining the above equations, we get an expression of the light deflection angle given by

$$\hat{\theta} = \left(\sqrt{1 - b^2 u_{\rm R}^2} + \sqrt{1 - b^2 u_{\rm S}^2}\right) \frac{2M}{b} - \left(\sqrt{1 - b^2 u_{\rm R}^2} - \sqrt{1 - b^2 u_{\rm S}^2}\right) \frac{2aM}{b^2} \\
- \left(\frac{1 - b^2 u_{\rm R}^2}{u_{\rm R}\sqrt{1 - b^2 u_{\rm R}^2}} + \frac{1 - b^2 u_{\rm S}^2}{u_{\rm S}\sqrt{1 - b^2 u_{\rm S}^2}}\right) \frac{b}{6} \frac{(1 - \hat{\alpha})}{8\pi c_{\rm O}} + \left(\frac{1}{\sqrt{1 - b^2 u_{\rm R}^2}} + \frac{1}{\sqrt{1 - b^2 u_{\rm S}^2}}\right) \frac{bM}{6} \frac{(1 - \hat{\alpha})}{8\pi c_{\rm O}} \\
+ \left(\frac{\sqrt{1 - b^2 u_{\rm R}^2}}{u_{\rm R}} + \frac{\sqrt{1 - b^2 u_{\rm S}^2}}{u_{\rm S}}\right) \frac{2a}{3} \frac{(1 - \hat{\alpha})}{8\pi c_{\rm O}} + \mathcal{O}\left[M^2, \left(\frac{1 - \hat{\alpha}}{8\pi c_{\rm O}}\right)^2, a^2\right]. \tag{72}$$

This form can be reduced to a simplified one using certain convenable approximations. Taking $u_S b << 1$ and $u_R b << 1$, we can get an expression involving divergent terms coupled to the cosmological contributions. These terms should be existed to show the cosmological background dependence. The desired deflection angle of light rays is found to be

$$\hat{\theta} = \frac{4M}{b} - \frac{4aM}{b^2} + \frac{bM}{3} \frac{(1-\hat{\alpha})}{8\pi c_{\rm O}} - \left(\frac{1}{u_{\rm R}} + \frac{1}{u_{\rm S}}\right) \frac{b}{6} \frac{(1-\hat{\alpha})}{8\pi c_{\rm O}} + \left(\frac{1}{u_{\rm R}} + \frac{1}{u_{\rm S}}\right) \frac{2a}{3} \frac{(1-\hat{\alpha})}{8\pi c_{\rm O}} + \mathcal{O}\left[M^2, \left(\frac{1-\hat{\alpha}}{8\pi c_{\rm O}}\right)^2, a^2\right]. (73)$$

An examination shows that this expression recovers many previous findings. Without the cosmological contributions, we get the results of the ordinary Symmergent black hole solutions investigated in [19].

In Fig. 8, we plotted Eqs. (72) (left) and (73) (right). The solid curves represent photons co-rotating with the black hole, while the dashed curves represent the counter-rotating photons. Remarkably, the co-rotating photons admit lower values of impact parameter b than when it is counter-rotating. For our chosen value of $\hat{\alpha} = 0.90$, $c_0 > 0$ causes the weak deflection angle to reach zero immediately as compared to $c_0 < 0$. For the latter, we can see that the weak deflection angle continuously increases as b further increases. In the right plot, as we consider a much farther observer, we note that the curves get more dispersed. Note that the values for c_0 are adjusted to decrease the magnitude of the Symmergent effect since its influence gets stronger for more remote observers. Even so, we can see the effect due to a much more remote observer, and the weak deflection angle has a higher value.

VI. PARTICLE ACCELERATION NEAR ROTATING SYMMERGENT BLACK HOLE BACKGROUNDS

Banãdos, Silk, and West (BSW) proved that a collision in an equatorial plane near the Kerr black hole could happen with an arbitrarily high center of mass-energy [111–113]. In this paper, we find that the Symmergent parameter c_0 has an important effect

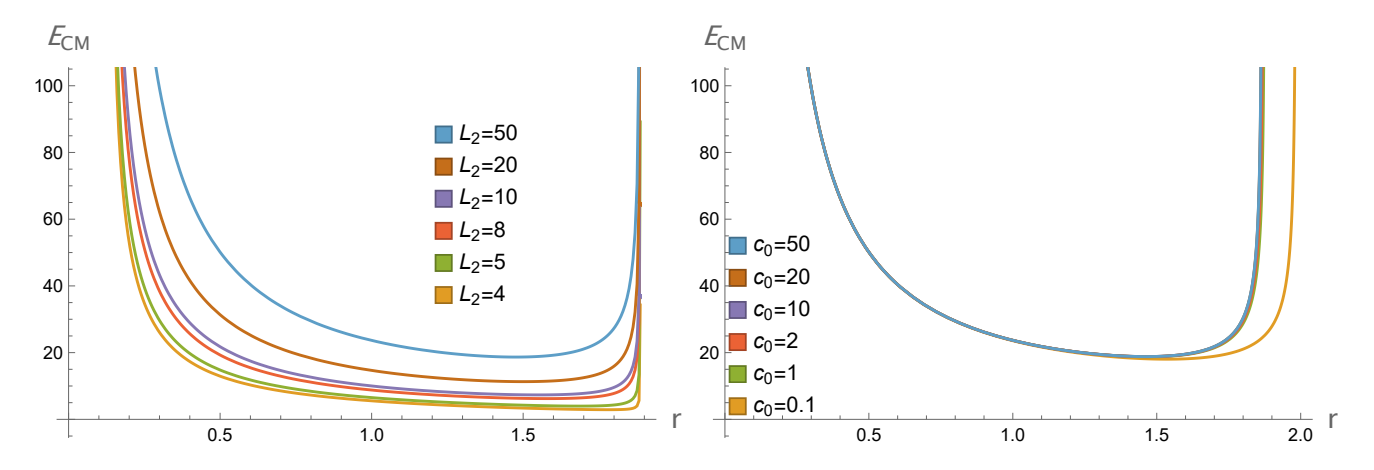


FIG. 9. Figures shows the variation of E_{cm} with radius for six combinations of L_2 (left figure) and c_0 (right figure) ($m = M = 1, L_1 = -4, \hat{\alpha} = 0.9$ and a = 0.5). We see that E_{cm} blows up at the horizons.

on the result. To do so, first we consider the particle motion on the equatorial plane $(\theta = \frac{\pi}{2}, \rho^2 = r^2)$. The generalized momenta P_{μ} can be written as follows:

$$P_{\mu} = g_{\mu\nu}\dot{x}^{\nu},\tag{74}$$

where the dot is for the derivative with respect to the affine parameter λ and $\mu, \nu = t, r, \phi, \theta$. Then one can write the generalized momenta P_t (test particle's energy per unit mass E) and P_{ϕ} (the angular momentum parallel to the symmetry axis per unit mass L):

$$P_t = g_{tt}\dot{t} + g_{t\phi}\dot{\phi},\tag{75}$$

$$P_{\phi} = g_{\phi\phi}\dot{\phi} + g_{t\phi}\dot{t}.\tag{76}$$

 P_t and P_{ϕ} are constants of motion.

To study the CM energy of the two-particle collision in the backgrounds of rotating Symmergent black holes, we write the expression of the CM energy E_{CM} of this two-particle collision: [111]

$$E_{\rm CM} = \sqrt{2}m_0\sqrt{1 - g_{\mu\nu}u_1^{\mu}u_2^{\nu}},\tag{77}$$

and

$$E_{\rm CM}^2 = 2m_0^2 \left(1 - g_{\mu\nu} u_1^{\mu} u_2^{\nu} \right) \tag{78}$$

where u_1^{μ}, u_2^{ν} are the 4-velocity vectors of the two particles $(u = (\dot{t}, \dot{r}, 0, \dot{\phi}))$.

Note that the angular momentums per unit mass of particle 1 and particle 2 are L_1, L_2 and their energies per unit mass E_1 and E_2 , respectively. We also consider the particles with the same rest mass m_0 . Initially the two particles are at rest at infinity $(E_1/m_0 = 1)$ and $E_2/m_0 = 1$) and then they approach the black hole and collide at a distance r.

Then one can obtain the CM energy as follows:

$$\bar{E}_{\text{CM}}^{2} = \frac{1}{2m_{0}^{2}} E_{\text{CM}}^{2} = \frac{1}{\Delta_{r} r^{2}} \left[\left(r^{2} + a^{2} \right)^{2} - a \left(L_{1} + L_{2} \right) \left(r^{2} + a^{2} - \Delta_{r} \right) + L_{1} L_{2} \left(a^{2} - \Delta_{r} \right) + \Delta_{r} \left(r^{2} - a^{2} \right) - X_{1} X_{2} \right], \tag{79}$$

with

$$X_{i} = \sqrt{(aL_{i} - r^{2} - a^{2})^{2} - \Delta_{r} \left((L_{i} - a)^{2} + \mu^{2} r^{2} \right)} \quad (i = 1, 2).$$
(80)

The collisions occur at the horizon of the black hole so that $\Delta_r = 0$ at Eq. (79). It is not difficult to see that the denominator of $\bar{E}_{\rm CM}^2$ is zero. Evidently, the maximal energy of the collision occurs if the values of L_1 and L_2 are opposite (such as head-on collision). It is seen from the Fig. 9, E_{cm} blows up at the horizons.

VII. CONCLUSION

In this paper, we have first investigated the effect of Symmergent gravity on the photonsphere, the black hole shadow, and the related observables. Our findings indicate that the location of the photonsphere depends on the Symmergent effects due to its coupling to the black hole spin parameter. We have seen how the unstable photon radii depend on c_0 , where its effect on the shadow size is reversed. The Symmergent gravity effect is evident, even for observers deviating from the equatorial plane. Interesting effects are also seen in the energy emission rate, which may directly affect the black hole's lifetime. Constraints on Symmergent parameters using the shadow radius data from the recent empirical results are also discussed. For different spin parameter a and the chosen value of $\hat{\alpha}=0.90$, a much lower values for c_0 under the $\pm 2\sigma$ at 95% confidence level were found in M87* than in Sgr. A*. The plot in Fig. 5 reveals that the detection of Symmergent effects can be achieved more easily in M87* than in Sgr. A*, for the clear reason that the farther the galaxy is, the stronger the Symmergent effects. Finally, for comparison, we also briefly analyzed such an effect on the time-like geodesic. Our findings indicate that massive particles are more sensitive to deviations caused by the Symmergent parameter than null particles.

Further in this paper, we investigated the Symmergent effects on photons' weak deflection angle as they traverse near the black hole. Further, we considered the finite distance effects. We have found out that not only the deflection depends on the sign of $c_{\rm O}$, but the deviations are also caused by how far the receiver is from the black hole. This effect is clearly shown in Fig. 8, where the parameters of $c_{\rm O}$ must be adjusted. It then implies that the weak deflection angle can detect Symmergent effects more easily for black holes that are so remote/distant relative to our location.

Lastly, we study the particle collision near the rotating Symmergent black hole background. We show that rotating Symmergent black holes can serve as particle accelerators because the center-of-mass energies blow up at the horizons. As a result, the BSW mechanism depends on the value of the Symmergent parameter $c_{\rm O}$ of the black hole.

Interesting research direction may include the investigation of the shadow and showing its dependence on the observer's state. One may also study the spherical photon orbits or the stability of time-like orbits.

ACKNOWLEDGMENTS

We thank Xiao-Mei Kuang for useful discussions. A. Ö. acknowledge hospitality at Sabancı University where this work was completed.

- [1] I. Çimdiker, D. Demir, and A. Övgün, Phys. Dark Univ. 34, 100900 (2021), 2110.11904.
- [2] A. Macias and A. Camacho, Phys. Lett. B 663, 99 (2008).
- [3] R. M. Wald, Einstein Stud. **14**, 439 (2018), 0907.0416.
- [4] F. Dyson, Int. J. Mod. Phys. A 28, 1330041 (2013).
- [5] G. 't Hooft and M. J. G. Veltman, Ann. Inst. H. Poincare Phys. Theor. A 20, 69 (1974).
- [6] A. D. Sakharov, Dokl. Akad. Nauk Ser. Fiz. 177, 70 (1967).
- [7] M. Visser, Mod. Phys. Lett. A 17, 977 (2002), gr-qc/0204062.
- [8] E. P. Verlinde, SciPost Phys. 2, 016 (2017), 1611.02269.
- [9] C. D. Froggatt and H. B. Nielsen, Annalen Phys. 517, 115 (2005), hep-th/0501149.
- [10] J. Polchinski, Nucl. Phys. B 231, 269 (1984).
- [11] H. Umezawa, J. Yukawa, and E. Yamada, Prog. Theor. Phys. 3, 317 (1948).
- [12] G. Kallen, Helv. Phys. Acta 22, 637 (1949).
- [13] D. Demir, Gen. Rel. Grav. 53, 22 (2021), 2101.12391.
- [14] D. Demir, Adv. High Energy Phys. 2019, 4652048 (2019), 1901.07244.
- [15] D. A. Demir, Adv. High Energy Phys. 2016, 6727805 (2016), 1605.00377.
- [16] N. D. Birrell and P. C. W. Davies, Quantum Fields in Curved Space, Cambridge Monographs on Mathematical Physics (Cambridge Univ. Press, Cambridge, UK, 1984), ISBN 978-0-521-27858-4, 978-0-521-27858-4.
- [17] D. Demir, Galaxies 9, 33 (2021), 2105.04277.
- [18] I. I. Çimdiker, Phys. Dark Univ. 30, 100736 (2020).
- [19] J. Rayimbaev, R. C. Pantig, A. Övgün, A. Abdujabbarov, and D. Demir (2022), 2206.06599.
- [20] K. S. Virbhadra and G. F. R. Ellis, Phys. Rev. D 62, 084003 (2000), astro-ph/9904193.
- [21] K. S. Virbhadra and G. F. R. Ellis, Phys. Rev. D 65, 103004 (2002).
- [22] V. Bozza, S. Capozziello, G. Iovane, and G. Scarpetta, Gen. Rel. Grav. 33, 1535 (2001), gr-qc/0102068.
- [23] V. Bozza, Phys. Rev. D 66, 103001 (2002), gr-qc/0208075.
- [24] V. Perlick, Phys. Rev. D 69, 064017 (2004), gr-qc/0307072.
- [25] G. He, X. Zhou, Z. Feng, X. Mu, H. Wang, W. Li, C. Pan, and W. Lin, Eur. Phys. J. C 80, 835 (2020).
- [26] G. W. Gibbons and M. C. Werner, Class. Quant. Grav. 25, 235009 (2008), 0807.0854.

- [27] A. Övgün, Phys. Rev. D 98, 044033 (2018), 1805.06296.
- [28] A. Övgün, Phys. Rev. D 99, 104075 (2019), 1902.04411.
- [29] A. Övgün, Universe 5, 115 (2019), 1806.05549.
- [30] W. Javed, R. Babar, and A. Övgün, Phys. Rev. D 100, 104032 (2019), 1910.11697.
- [31] M. C. Werner, Gen. Rel. Grav. 44, 3047 (2012), 1205.3876.
- [32] A. Ishihara, Y. Suzuki, T. Ono, T. Kitamura, and H. Asada, Phys. Rev. D 94, 084015 (2016), 1604.08308.
- [33] A. Ishihara, Y. Suzuki, T. Ono, and H. Asada, Phys. Rev. D 95, 044017 (2017), 1612.04044.
- [34] T. Ono, A. Ishihara, and H. Asada, Phys. Rev. D 96, 104037 (2017), 1704.05615.
- [35] R. C. Pantig and E. T. Rodulfo, Chin. J. Phys. 66, 691 (2020), 2003.00764.
- [36] R. C. Pantig, P. K. Yu, E. T. Rodulfo, and A. Övgün, Annals of Physics 436, 168722 (2022), 2104.04304.
- [37] R. C. Pantig and A. Övgün, Eur. Phys. J. C 82, 391 (2022), 2201.03365.
- [38] R. C. Pantig and A. Övgün (2022), 2202.07404, URL https://arxiv.org/abs/2202.07404.
- [39] Z. Li and A. Övgün, Phys. Rev. D **101**, 024040 (2020), 2001.02074.
- [40] Z. Li, G. Zhang, and A. Övgün, Phys. Rev. D **101**, 124058 (2020), 2006.13047.
- [41] A. Belhaj, H. Belmahi, M. Benali, and H. Moumni El (2022), 2204.10150.
- [42] S. Vagnozzi, R. Roy, Y.-D. Tsai, and L. Visinelli (2022), 2205.07787.
- [43] Y. Chen, R. Roy, S. Vagnozzi, and L. Visinelli (2022), 2205.06238.
- [44] R. C. Pantig and E. T. Rodulfo, Chinese J. Phys. **68**, 236 (2020).
- [45] I. Dymnikova and K. Kraav, Universe 5, 1 (2019), ISSN 22181997.
- [46] R. C. Pantig and A. Övgün (2022), 2202.07404.
- [47] A. Uniyal, R. C. Pantig, and A. Övgün (2022), 2205.11072.
- [48] X.-M. Kuang and A. Övgün (2022), 2205.11003.
- [49] Y. Meng, X.-M. Kuang, and Z.-Y. Tang (2022), 2204.00897.
- [50] Z.-Y. Tang, X.-M. Kuang, B. Wang, and W.-L. Qian (2022), 2206.08608.
- [51] X.-M. Kuang, Z.-Y. Tang, B. Wang, and A. Wang (2022), 2206.05878.
- [52] R. C. Pantig and A. Övgün (2022), 2206.02161, URL https://arxiv.org/abs/2206.02161.
- [53] S.-W. Wei, Y.-C. Zou, Y.-X. Liu, and R. B. Mann, JCAP 08, 030 (2019), 1904.07710.
- [54] Z. Xu, X. Hou, and J. Wang, JCAP 10, 046 (2018), 1806.09415.
- [55] X. Hou, Z. Xu, and J. Wang, JCAP 12, 040 (2018), 1810.06381.
- [56] C. Bambi, K. Freese, S. Vagnozzi, and L. Visinelli, Phys. Rev. D 100, 044057 (2019), 1904.12983.
- [57] N. Tsukamoto, Phys. Rev. D 97, 064021 (2018), 1708.07427.
- [58] R. Kumar, S. G. Ghosh, and A. Wang, Phys. Rev. D 101, 104001 (2020), 2001.00460.
- [59] R. Kumar, S. G. Ghosh, and A. Wang, Phys. Rev. D 100, 1 (2019), ISSN 24700029, 1912.05154.
- [60] M. Wang, S. Chen, and J. Jing, J. Cosmol. Astropart. Phys. 2017, 1 (2017), ISSN 14757516, 1707.09451.
- [61] M. Wang, S. Chen, and J. Jing, Phys. Rev. D 98, 1 (2018), ISSN 24700029, 1801.02118.
- [62] L. Amarilla and E. F. Eiroa, 14th Marcel Grossman Meet. Recent Dev. Theor. Exp. Gen. Relativ. Astrophys. Relativ. F. Theor. Proc. -, 3543 (2018), 1512.08956.
- [63] H. Peng-Zhang, F. Qi-Qi, Z. Hao-Ran, and D. Jian-Bo, Eur. Phys. J. C 80, 1195 (2020).
- [64] O. Y. Tsupko, Z. Fan, and G. S. Bisnovatyi-Kogan, Class. Quant. Grav. 37, 065016 (2020), 1905.10509.
- [65] K. Hioki and K.-i. Maeda, Phys. Rev. D 80, 024042 (2009), 0904.3575.
- [66] R. A. Konoplya, Phys. Lett. B 795, 1 (2019), 1905.00064.
- [67] R. C. Pantig, in Proceedings of the Samahang Pisika ng Pilipinas (2021), vol. 39, pp. SPP-2021-1C-03.
- [68] M. Okyay and A. Övgün, JCAP **01**, 009 (2022), 2108.07766.
- [69] A. Belhaj, M. Benali, A. El Balali, H. El Moumni, and S. E. Ennadifi, Class. Quant. Grav. 37, 215004 (2020), 2006.01078.
- [70] P.-C. Li, M. Guo, and B. Chen, Phys. Rev. D **101**, 084041 (2020), 2001.04231.
- [71] R. Ling, H. Guo, H. Liu, X.-M. Kuang, and B. Wang, Phys. Rev. D 104, 104003 (2021), 2107.05171.
- [72] A. Belhaj, H. Belmahi, M. Benali, W. El Hadri, H. El Moumni, and E. Torrente-Lujan, Phys. Lett. B 812, 136025 (2021), 2008.13478.
- [73] P. V. P. Cunha and C. A. R. Herdeiro, Gen. Rel. Grav. 50, 42 (2018), 1801.00860.
- [74] S. E. Gralla, D. E. Holz, and R. M. Wald, Phys. Rev. D 100, 024018 (2019), 1906.00873.
- [75] V. Perlick, O. Y. Tsupko, and G. S. Bisnovatyi-Kogan, Phys. Rev. D 92, 104031 (2015), 1507.04217.
- [76] P. G. Nedkova, V. K. Tinchev, and S. S. Yazadjiev, Phys. Rev. D 88, 124019 (2013), 1307.7647.
- [77] Z. Li and C. Bambi, JCAP 01, 041 (2014), 1309.1606.
- [78] M. Khodadi, G. Lambiase, and D. F. Mota, JCAP 09, 028 (2021), 2107.00834.
- [79] M. Khodadi and G. Lambiase (2022), 2206.08601.
- [80] P. V. P. Cunha, C. A. R. Herdeiro, B. Kleihaus, J. Kunz, and E. Radu, Phys. Lett. B 768, 373 (2017), 1701.00079.
- [81] R. Shaikh, Phys. Rev. D 100, 024028 (2019), 1904.08322.
- [82] A. Allahyari, M. Khodadi, S. Vagnozzi, and D. F. Mota, JCAP 02, 003 (2020), 1912.08231.
- [83] A. Yumoto, D. Nitta, T. Chiba, and N. Sugiyama, Phys. Rev. D 86, 103001 (2012), 1208.0635.
- [84] P. V. P. Cunha, C. A. R. Herdeiro, E. Radu, and H. F. Runarsson, Int. J. Mod. Phys. D 25, 1641021 (2016), 1605.08293.
- [85] J. W. Moffat, Eur. Phys. J. C 75, 130 (2015), 1502.01677.
- [86] P. V. P. Cunha, J. Grover, C. Herdeiro, E. Radu, H. Runarsson, and A. Wittig, Phys. Rev. D 94, 104023 (2016), 1609.01340.
- [87] A. F. Zakharov, Phys. Rev. D 90, 062007 (2014), 1407.7457.
- [88] R. A. Hennigar, M. B. J. Poshteh, and R. B. Mann, Phys. Rev. D 97, 064041 (2018), 1801.03223.
- [89] L. Chakhchi, H. El Moumni, and K. Masmar, Phys. Rev. D 105, 064031 (2022).

- [90] J. L. Synge, Mon. Not. R. Astron. Soc. 131, 463 (1966), ISSN 0035-8711.
- [91] J. P. Luminet, Astron. Astrophys. 75, 228 (1979).
- [92] J. M. Bardeen, in Les Houches Summer School of Theoretical Physics: Black Holes (1973), pp. 215-240.
- [93] S. Chandrasekhar, The mathematical theory of black holes (Oxford University Press., New York, 1998).
- [94] B. P. Abbott et al. (LIGO Scientific, Virgo), Phys. Rev. Lett. 116, 061102 (2016), 1602.03837.
- [95] K. Akiyama et al. (Event Horizon Telescope), Astrophys. J. Lett. 875, L6 (2019), 1906.11243.
- [96] K. Akiyama et al. (Event Horizon Telescope), Astrophys. J. Lett. 930, L12 (2022).
- [97] J. A. R. Cembranos, A. de la Cruz-Dombriz, and P. Jimeno Romero, Int. J. Geom. Meth. Mod. Phys. 11, 1450001 (2014), 1109.4519.
- [98] D. Perez, G. E. Romero, and S. E. P. Bergliaffa, Astron. Astrophys. 551, A4 (2013), 1212.2640.
- [99] A. G. Suvorov, Phys. Rev. D 99, 124026 (2019), 1905.02021.
- [100] Y. S. Myung, Phys. Rev. D 88, 104017 (2013), 1309.3346.
- [101] G. L. L. Nashed and S. Nojiri, JCAP 11, 007 (2021), 2109.02638.
- [102] G. G. L. Nashed, Phys. Lett. B 815, 136133 (2021), 2102.11722.
- [103] G. W. Gibbons, M. J. Perry, and C. N. Pope, Class. Quant. Grav. 22, 1503 (2005), hep-th/0408217.
- [104] Z. Gao, X. Kong, and L. Zhao, Eur. Phys. J. C 82, 112 (2022), 2112.08672.
- [105] P. Slany and Z. Stuchlik, Eur. Phys. J. C 80, 587 (2020).
- [106] B. Carter, Phys. Rev. 174, 1559 (1968).
- [107] T. Johannsen, Astrophys. J. 777, 170 (2013).
- [108] K. Akiyama et al. (Event Horizon Telescope), Astrophys. J. Lett. 875, L1 (2019), 1906.11238.
- [109] B. Bautista-Olvera, J. C. Degollado, and G. German, arXiv preprint arXiv:1908.01886 pp. 1–18 (2019), 1908.01886.
- [110] P. Slaný, M. Pokorná, and Z. Stuchlík, Gen. Relativ. Gravit. 45, 2611 (2013), ISSN 00017701, 0307049.
- [111] M. Banados, J. Silk, and S. M. West, Phys. Rev. Lett. 103, 111102 (2009), 0909.0169.
- [112] M. Halilsoy and A. Ovgun, Adv. High Energy Phys. 2017, 4383617 (2017), 1504.03840.
- [113] M. Halilsoy and A. Ovgun, Can. J. Phys. 95, 1037 (2017), 1507.00633.